Tailoring Fe-Base Alloys for Intermediate Temperature SOFC Interconnect Application

A Final Technical Report

for

DOE Award No. DE-FC26-04NT42223

Oct. 1, 2004 – Dec. 31, 2007

Submitted by

J. H. Zhu

Department of Mechanical Engineering, Box 5014
Tennessee Technological University, Cookeville, TN 38505

M. P. Brady

Metals and Ceramics Division
Oak Ridge National Laboratory, Oak Ridge, TN 37831

H. U. Anderson

Electrical Materials Applied Research Center
University of Missouri-Rolla, Rolla, MO 65409

ABSTRACT

This report summarized the research efforts and major conclusions for our SECA Phase I and II project focused on Cr-free or low Cr Fe-Ni based alloy development for intermediate temperature solid oxide fuel cell (SOFC) interconnect application. Electrical conductivity measurement on bulk $(Fe,Ni)_3O_4$ coupons indicated that this spinel phase possessed a higher electrical conductivity than $Cr_{1.5}Mn_{1.5}O_4$ spinel and Cr_2O_3, which was consistent with the low area specific resistance (ASR) of the oxide scale formed on these Fe-Ni based alloys. For Cr-free Fe-Ni binary alloys, although the increase in Ni content in the alloys improved the oxidation resistance, and the Fe-Ni binary alloys exhibited adequate CTE and oxide scale ASR, their oxidation resistance needs to be further improved. Systematic alloy design efforts have led to the identification of one low-Cr (6wt.%) Fe-Ni-Co based alloy which formed a protective, electrically-conductive Cr_2O_3 inner layer underneath a Cr-free, highly conductive spinel outer layer. This low-Cr, Fe-Ni-Co alloy has demonstrated a good CTE match with other cell components; high oxidation resistance comparable to that of Crofer; low oxide scale ASR with the formation of electrically-insulating phases in the oxide scale; no scale spallation during thermal cycling; adequate compatibility with cathode materials; and comparable mechanical properties with Crofer. The existence of the Cr-free $(Fe,Co,Ni)_3O_4$ outer layer effectively reduced the Cr evaporation and in transpiration testing resulted in a 6-fold decrease in Cr evaporation as compared to a state-of-the-art ferritic interconnect alloy. In-cell testing using an anode supported cell with a configuration of Alloy/Pt/LSM/YSZ/Ni+YSZ indicates that the formation of the Cr-free spinel layer via thermal oxidation was effective in blocking the Cr migration and thus improving the cell performance stability. Electroplating of the Fe-Ni-Co alloys as precursor to synthesize a protective spinel layer on commercial ferritic steels has been initiated to facilitate the utilization of the Cr-free spinel as a surface seal to block Cr evaporation. It is suggested that low-cost Fe-Ni-Co alloy coating on commercial ferritic steels might be the best approach to completely eliminate the Cr poisoning problem in SOFC stacks, while maintaining the relatively low overall cost of the interconnect component.

TABLE OF CONTENTS

1. Executive Summary

This final scientific/technical report summarized the research efforts and major conclusions for the SECA Project "Tailoring Fe-Ni Base Alloys for Intermediate-Temperature SOFC Interconnect Application", for the period of Oct. 1, 2004 – Dec. 31, 2007. This interdisciplinary project is a collaborative research endeavor between Tennessee Technological University (TTU), Oak Ridge National Laboratory (ORNL), and University of Missouri – Rolla (UMR), aiming at developing a new class of Cr-free or low Cr, Fe-Ni alloys as interconnect material for intermediate-temperature SOFC stacks.

For the Cr-free binary Fe-Ni alloys, the composition of the spinel phase in the oxide scale was found to be close to $Ni_{0.9}Fe_{2.1}O_4$. Electrical conductivity measurement on a bulk spinel coupon with similar composition indicated that this spinel phase exhibited much higher electrical conductivity than both $Cr_{1.5}Mn_{1.5}O_4$ and Cr_2O_3, which was consistent with the low area specific resistance of the oxide scales formed on these binary Fe-Ni alloys. Also, off-stoichiometric spinel $Ni_{0.9}Fe_{2.1}O_4$ possessed a higher electrical conductivity than the stoichiometric spinel $NiFe_2O_4$, while doping with transition metals such as Co and Mn or reactive elements such as La and Y further improved the electrical conductivity of $Ni_{0.9}Fe_{2.1}O_4$. Oxidation kinetics study showed that as the oxidation temperature increased, the weight gain of the Fe-50Ni-0.05Y alloy in air increased more rapidly, while no weight change was observed during exposure to Ar+4%H_2 saturated with water. The increase in Ni content from 40 to 60 wt% in the Fe-Ni alloys improved the oxidation resistance, most likely via the enhanced formation of a NiO layer between the spinel and substrate. The thermal expansion behavior and area specific resistance of these Fe-Ni alloys were comparable to the commercial interconnect alloys such as Crofer, Ebrite, and Haynes 230. Even though these binary Fe-Ni alloys showed overall promising performance in SOFC operation conditions, their oxidation resistance is not adequate and needs to be improved.

Through a systematic alloy design effort, a low Cr (6wt.%Cr) Fe-Ni-Co based alloy with drastically improved oxidation resistance has been developed. For this low Cr Fe-Ni-Co based alloy, a double-layer oxide structure with a Cr-free, electrically-conductive spinel outer layer and protective Cr_2O_3 inner layer was established after thermal oxidation. This low-Cr, Fe-Ni alloy demonstrated a good CTE match with other cell components; high oxidation resistance comparable to that of Crofer; low oxide scale ASR; no scale spallation during thermal cycling; and adequate compatibility with cathode material $(La,Sr)MnO_3$. The oxidation resistance improvement is due to the formation of the continuous Cr_2O_3 inner layer, while the low scale ASR is a result of the formation of a highly-conductive spinel outer layer. The excellent scale spallation resistance can be attributed to the close match in CTE between the spinel scale and the substrate alloy. The existence of the Cr-free $(Fe,Co,Ni)_3O_4$ outer layer effectively reduced the Cr evaporation

and in transpiration testing resulted in a 6-fold decrease in Cr evaporation as compared to a state-of-the-art ferritic interconnect alloy.

In-cell testing using an anode supported cell with a configuration of Alloy/Pt/LSM/YSZ/Ni+YSZ clearly indicates that the formation of the Cr-free spinel layer via thermal oxidation of the new alloy was effective in blocking the Cr migration and thus improving the cell performance stability. Furthermore, the tensile testing from room temperature to 900°C of the new alloy indicates that its ductility is similar to Crofer 22 APU up to 600°C and slightly lower in the range of 600-900°C, while the new alloy exhibits a much higher yield strength and tensile strength than Crofer 22 APU over the entire test temperature range.

A new research direction on electroplating of Fe-Ni-Co alloys as precursor to synthesize a protective spinel layer on ferritic steels has been initiated. It is suggested that low-cost Fe-Ni-Co alloy coating on commercial ferritic steels might be the best approach to completely eliminate the Cr poisoning problem in SOFC stacks, while maintaining the relatively low cost of the metallic interconnect component. The new alloy/coating system is expected to reduce the overall cost and improve the durability of SOFC stacks, thus contributing to early commercialization of the SOFC technology.

2. Introduction

Some major technical challenges such as cost-effective manufacturing and long-term reliability of the stack must be overcome to advance the SOFC technology to commercial reality. One of these critical issues is the development of a suitable interconnect materials that provide electrical series connection of individual single cells and gas impermeability to separate fuel and oxidant gases. A significant advance in the development of intermediate temperature SOFCs has been the use of metallic materials as interconnects [1-10]. They present several advantages compared to the ceramic interconnect: lower cost, easier manufacture, better workability, improved mechanical strength of the stack, higher electronic conductivity and higher thermal conductivity (more uniform heat distribution). Two major concerns for metallic interconnects are their oxidation resistance and oxide scale electrical conductivity. The high temperature oxidation resistant alloys include Al_2O_3-, SiO_2- and Cr_2O_3- forming alloys. However, Cr_2O_3-forming alloys are preferred for interconnect; since only Cr_2O_3 shows adequate electrical conductivity under SOFC operating conditions, whereas both Al_2O_3 and SiO_2 are electronically insulating. Therefore, all of the current candidates of metallic interconnect are Cr_2O_3-forming alloys. However, the Cr_2O_3-forming alloys have an inherent weakness that is the formation of volatile Cr(VI) species under operating environments of SOFC due to Cr_2O_3 evaporation [11]. Volatile Cr(VI) may migrate and poison the cathode, leading to the decreased electrochemical activity of the cathode and the degradation in SOFC system performance over long-term operation [12]. Surface coatings with less Cr volatility might reduce the severity of these Cr evaporation problems, but it would be difficult to completely mitigate this issue, by surface coatings alone. To reduce the Cr volatility, Mn was added purposely in the new ferritic alloy Crofer, to facilitate the formation of a double-layer structure of $(Mn,Cr)_3O_4$ spinel outer-layer and Cr_2O_3 inner-layer during thermal exposure [13-15]. The presence of the spinel outer layer indeed reduced the Cr evaporation rate; however, the Cr evaporation was still not completely eliminated [16]. Furthermore, Mn addition lowered the oxidation resistance of the ferritic alloy. Clearly, further alloy design efforts are needed to improve the overall performance of metallic interconnect alloys.

In this SECA project, we have focused on developing Cr-free or low Cr, Fe-Ni base alloys as new SOFC interconnect materials. The Fe-Ni alloys with about 40-60 wt.% Ni are expected to have suitable match in coefficient of thermal expansion (CTE) with other cell components. For example, the CTE of the Fe-50Ni and Fe-50Ni-6Cr-0.05Y alloys (all alloy compositions given in this report are in wt.%) is close to that of other cell components as shown in Fig.1 [17]. Furthermore, these Fe-Ni alloys are Cr-free or low Cr, which is desirable to eliminate the Cr poisoning problem in SOFC stacks. Our overall strategy is to utilize alloy design principles to fine-tune the compositions of these Fe-Ni-Co alloys such that a double-layer surface oxide structure will be thermally grown on these alloys with a Cr-free, electrically-conductive $(Fe,Ni)_3O_4$ spinel outer-layer as a surface seal for Cr evaporation and an electrically-conductive, oxidation-resistant inner-layer to provide adequate oxidation resistance and oxide scale electrical conductivity, as shown schematically in Fig.2. An interdisciplinary and collaborative endeavor, has been

undertaken, with particular expertise in the areas of metallurgical engineering (TTU), ceramic engineering (UMR), electrochemistry (TTU/UMR), and oxidation/corrosion science (ORNL/TTU). In this final technical report, we summarized the major results and findings of our project, which demonstrated the feasibility to form the double-layer oxide structure, the suitability of the electrical conductivity of $(Fe,Ni)_3O_4$ spinel, and the promises offered by the Fe-Ni-Co alloy system. Furthermore, the new alloy system that we developed under this project has been systematically evaluated and the future research direction for this project has been identified.

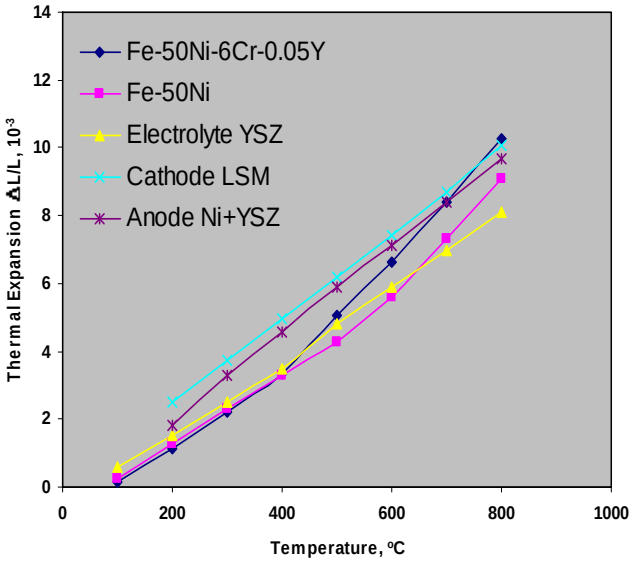

Fig.1 Thermal expansion vs. temperature for the Fe-50Ni-6Cr-0.05Y alloy (wt.%), as compared to other cell components

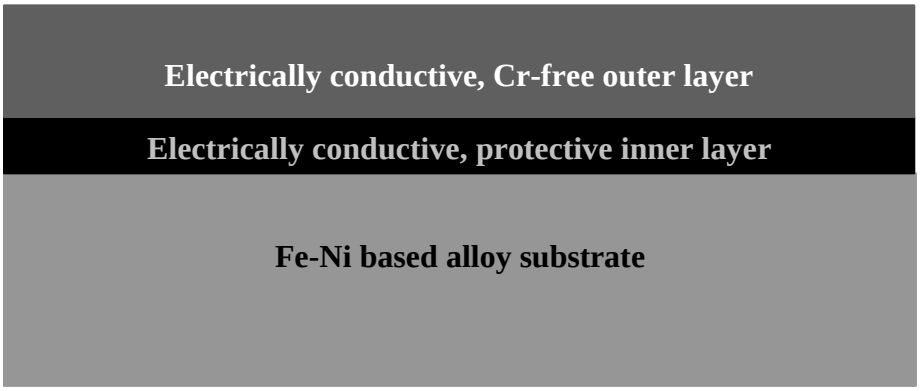

Fig.2 Schematic of the desirable double-layer oxide structure for Fe-Ni based alloys

3. Experimental Procedures

3.1 Materials Preparation

All the Fe-Ni and Fe-Ni-Co containing alloys were prepared by arc-melting and drop-casting in a chilled copper mold, starting with high-purity elements. Each ingot weighing

about 50-120 grams was melted 6 times to ensure compositional homogeneity. After casting, the top parts were cut off and the remaining rectangular pieces with a dimension of 12×12×50mm were given a homogenization heat treatment at 1100ºC in vacuum (about 10^{-6} torr) for 10 hours, followed by furnace cooling. Some of the alloy ingots were hot rolled at 1000ºC repeatedly to sheets with thickness of about 1.5mm. The alloy ingots were cut into desirable dimensions for oxidation test and thermal expansion measurement. For transpiration experiment, larger ingots (500 grams) were also prepared and rolled to 1.5 mm strips; these strips have been ground to 600-grit, clean-surface finish with a final thickness of 1 mm. Cr transpiration measurement was conducted at PNNL.

$NiFe_2O_4$ and $Ni_{0.9}Fe_{2.1}O_4$ powders, as well as $Ni_{0.9}Fe_{2.1}O_4$ powders doped with various transition metals and reactive elements, were synthesized via a glycine-nitrate process (GNP) first described by L. A. Chick et al [18]. $Ni(NO_3)_2{\cdot}6H_2O$ (Alfa Aesar®, 99.9985% pure), $Fe(NO_3)_3{\cdot}9H_2O$ (Sigma-Aldrich, 99.99+% pure) and other desired metal nitrate were dissolved into distilled water in an appropriate ratio, glycine (Alfa Aesar®, 99.5% pure) was then added into the solution as a chelating agent and fuel. The solution was slowly heated and stirred at about 80ºC to expel the water until a gel was obtained. The gel was burned in a stainless steel beaker. The as-synthesized powders were calcined at 900ºC for 5 hours to burn out the remaining organics and form the spinel phase. The powders were ball milled for 30 min and then pressed into pellets with 1" or 2" diameter. These pellets were sintered and densified at 1500ºC for 4 hours. X-ray diffraction (XRD) results confirmed that for all the specimens a single phase with spinel structure was present after sintering at 1500ºC for 4 hours.

3.2 Oxidation Tests and Oxide Scale Analysis

Rectangular samples of 12×12×(1-2) mm were cut from the ingots by a precision saw or electronic-discharge machining (EDM). After drilling a 1-mm diameter hole in the upper center, each sample was ground up to 800 grits with SiC sand paper, ultrasonically cleansed in acetone, and then dried for evaluation. The short-term isothermal oxidation tests of the alloys were carried out in a Cahn thermobalance with a linear heating rate of 75ºC/min to study its oxidation kinetics. The samples were continuously oxidized for 30 hours at 700, 800, and 900ºC in flowing air (the flowing rate is 45ml/min) or Ar+4%H_2 saturated with water (i.e. Ar+H_2+H_2O). The mass gain of the sample was recorded as a function of time, after the sample temperature was raised to the oxidation temperature.

Longer-term oxidation tests of these alloys were also conducted. For isothermal oxidation test, the samples were hung in alumina crucibles, oxidized for 500 hours at 800ºC in air, followed by furnace cooling; or oxidized for three weeks at 800ºC in air (for each week, holding one week at 800ºC in air, followed by furnace cooling). Some samples were also cyclically oxidized to evaluate the oxide scale adhesion, each cycle consisting of isothermal holding at 800ºC in air for 25 hours and then cooling to room temperature.

The phase structure of the oxide scale formed on the alloys was identified with X-ray diffraction (XRD). The surface morphologies and cross-sections of the oxidized samples were observed using scanning electron microscopy (SEM) attached with an energy-

dispersive X-ray spectroscopy (EDS). The compositions of the oxide scale were determined using electron probe microanalysis (EPMA).

Scanning transmission electron microscopy (STEM) was used to verify the oxide scale microstructures formed on the newly-developed low-Cr Fe-Co-Ni alloy after thermal exposure at 800ºC in air for 3 weeks. STEM samples were prepared by the focused-ion beam (FIB) technique at ORNL. STEM images of the regions near the interfaces between the $(Fe,Ni,Co)_3O_4$ outer layer and the Cr_2O_3 region as well as between the internal oxidation zone and the alloy substrate were obtained and the chemical compositions of the oxide phases in the scale were determined by energy-dispersive spectroscopy (EDS) attached with the STEM.

3.3 Measurement of Electrical Property

Electrical resistance of the oxidized samples was measured using the 2-probe 4-point method from 500 to 800ºC [19]. For electrical resistance measurement, two of the oxidized surfaces were covered with Pt paste, and Pt meshes attached with four Pt leads were placed on top of the pastes for current collection. A constant current (I) was applied across two Pt leads using a power source, the corresponding voltage drop (V) across the other two Pt leads was then measured using a multimeter. In this experiment, the variation of voltage (V) across the samples under different currents (I) ranging from 1 to 100 mA was verified to follow the Ohm's law exactly, which indicated that the interfacial polarization was negligible with the applied current range. A constant current of 10 mA was used in all of the measurement reported in this report. The electrical resistance of the samples at the same temperature was measured twice upon heating and cooling, respectively, which generally showed good agreement. A widely accepted parameter for scaling the electrical resistance of the oxide scales, area specific resistance (ASR), was reported here. It should be noted that ASR reflected both the electrical conductivity and the thickness of the oxide scale. At each temperature, the resistance (R) was calculated according to the Ohm's law, R=V/I. the ASR was then equal to R multiplied by the area that the Pt paste covered.

For electrical conductivity measurement of the spinel phase, the sintered specimens were cut into bars and ground into specific dimensions. A thin layer of platinum paste was applied on two ends of the specimens to keep good contact between specimens and platinum wires. A 4-probe measurement was employed to determine the electrical conductivity of the spinels. A constant current was provided by a current source in all measurements and the voltage drop across the two inner probes was measured with a multimeter for the electrical conductivity calculation.

3.4 Thermal Expansion Measurement and Alloy/Cathode Compatibility Study

Thermal expansion behaviors of the alloys and the spinel oxides were determined with a dilatometer with either round or rectangular bars. The measurement was conducted from 20 to 800ºC in ambient air.

For the compatibility test of these Fe-Ni and Fe-Ni-Co alloys with typical SOFC cathode material (La,Sr)MnO_3 (LSM), an LSM layer of about 20-30μm thick was screen printed onto the polished alloy coupons to form alloy/cathode couples. These couples were held at 900°C hours in air for 300 hours. ASR measurements of these couples were conducted to get the overall resistance of the alloy/cathode couple after the high-temperature treatment. Cross-sectional metallographic samples were then prepared by sectioning, grinding, and polishing of these couples. EPMA was used to determine the distribution of various elements in the couples, with special attentions paid to the alloy/cathode interface as well as possible Cr migration to the cathode.

3.5 Cr Transport Measurement and In-cell Testing

Cr volatility was measured quantitatively by flowing moist air across alloy samples in a tube furnace. Volatilized Cr was transported by the air stream to the cold end of the fused silica tube where it condensed on the tube surface and on collection media. The air stream was also taken through a condenser and water bubbler to assure complete Cr collection. When the experiment was complete, nitric acid rinses were used to dissolve the collected Cr-containing condensate from the tube and collection media. This rinsate was combined with the water from the bubbler and analyzed by ICP-mass spectrometry to quantitatively determine the amount of Cr volatilized during the test. Cr transport rates ($kg \cdot m^{-2} \cdot s^{-1}$) were determined by dividing the total mass of Cr volatilized by the exposed surface area of the alloy samples and the total time of exposure at temperature. The Cr transport measurement was conducted at Pacific Northwest National Laboratory.

In addition, the performance stability of a solid oxide fuel cell (SOFC) was studied with the new alloy as interconnect. The cell configuration included a porous Ni/YSZ anode substrate as support, a Ni/YSZ anode interlayer, a thin YSZ electrolyte layer, a LSM/YSZ cathode interlayer, and a LSM cathode, and a Pt layer for cathode-interconnect contact, and a channeled alloy interconnect. The cell testing was conducted at 1073K using H_2+3%H_2O gas as fuel and the current density of the cell was monitored as a function of time at a fixed cell voltage of 0.7V. Crofer 22 APU was also tested for comparison. The effect of preoxidation of the new alloy (800ºC for 120 h in air) as well as an electroplated Co-Fe alloy coating on the cell performance was also evaluated.

3.6 Tensile Property Measurement

The tensile properties of the new alloy were determined as a function of test temperature. Tensile specimens with gauge sections of 0.7 x 3 x 13 mm were electric-discharge machined from the sheets. The specimens were hand polished through 600 grit SiC paper. Tensile tests were conducted on a screw-driven *Instron* tensile machine equipped with a vacuum chamber. The chamber was first evacuated to a pressure of ~$7x10^{-4}$ Pa prior to testing and was being continuously pumped during the test. The test temperature varied from room temperature to 900ºC. All specimens were tested at a nominal strain rate of $3.4x10^{-3}$ s^{-1}.

4. Results and Discussions

4.1 Cr-free Fe-Ni Binary Alloys

4.1.1 Thermal Expansion Behavior

Fig.3 shows the thermal expansion behaviosr of Fe-Ni binary alloys with different Ni levels (45-60wt.%). Although the CTE of Fe-Ni binary alloys increased with the increase of Ni content in alloys, the thermal expansion behavior of these alloys was moderately close to that of other cell components.

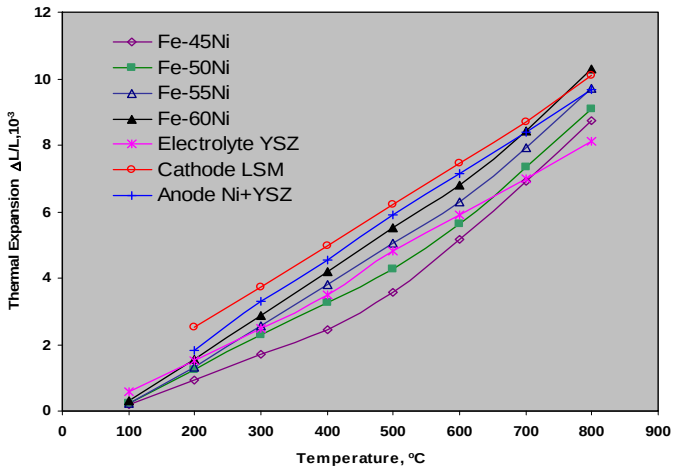

Fig.3 Thermal expansion vs. temperature for the Fe-Ni alloys with different Ni content (wt.%), as compared to other cell components

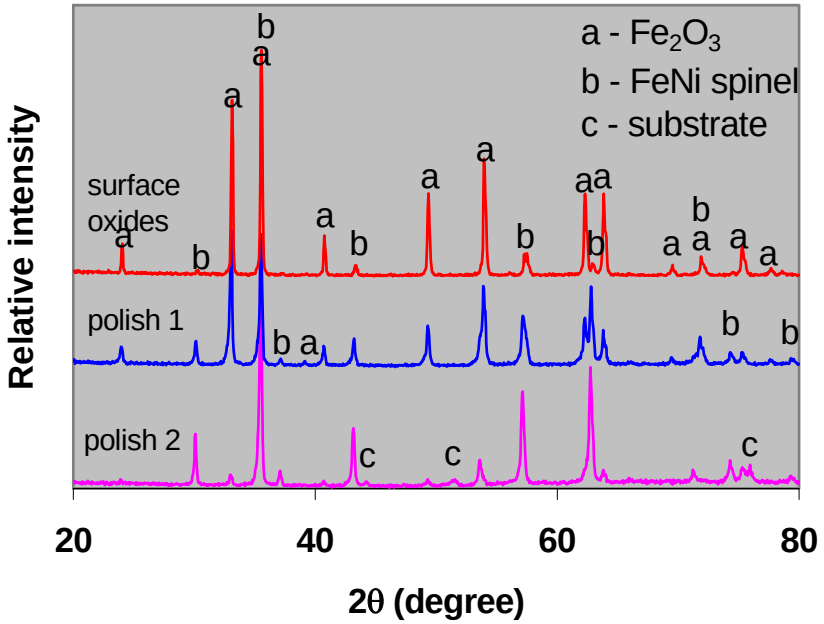

Fig. 4 XRD patterns of different oxide layers formed on Fe-50Ni-0.05Y after oxidation for 500 hours in air at 800°C: (1) in as-oxidized condition (no polish); (2) after slight polishing (polish 1); and (3) after further polishing (polish 2)

4.1.2 Oxidation Behavior and Oxide Scale ASR

Alloy coupons of Fe-50Ni-0.05Y (wt.%) were oxidized for 500 hours in air at 800°C. In order to determine the phases present at different locations in the oxide scale, one oxidized sample was slightly polished step by step after oxidation, and the X-ray diffraction patterns were taken correspondingly, as shown in Fig.4. The oxide scale consisted of Fe_2O_3 and $(Fe,Ni)_3O_4$ spinel. The peak intensity from Fe_2O_3 became weaker while the peak intensity from $(Fe,Ni)_3O_4$ spinel became stronger with polishing. It is therefore concluded that the oxide scale formed on Fe-50Ni-0.05Y consisted mainly of an Fe_2O_3 outer layer and an $(Fe,Ni)_3O_4$ spinel inner layer.

EMPA was used to determine the composition of the $(Fe,Ni)_3O_4$ spinel formed after oxidation, as shown in Fig.5. Fig.5 (a) is an SEM image of the cross section of the oxidized coupon, while Fig.5 (b) is the corresponding compositional profile across the line indicated in Fig.5 (a). Consistent with the XRD results, an $(Fe,Ni)_3O_4$ spinel layer was formed between the alloy substrate and the Fe_2O_3 outer layer. The atomic percentage (at.%) of Fe, Ni and O in the spinel was shown in Table 1, which was close to $Ni_{0.9}Fe_{2.1}O_4$.

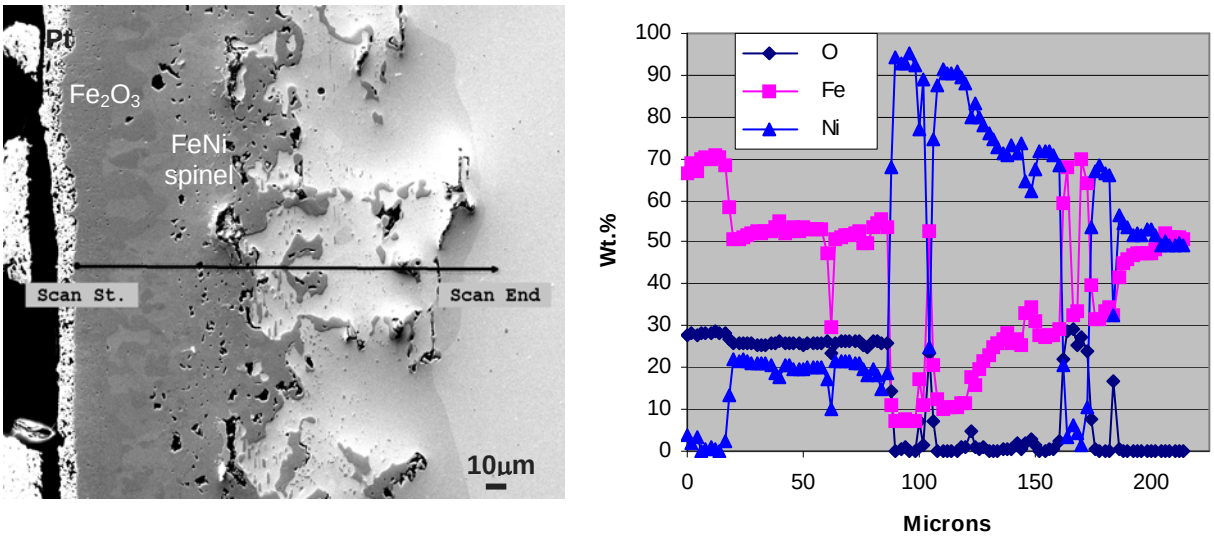

(a) (b)

Fig.5 SEM Cross-sectional image (a) and EPMA results (b) of Fe-50Ni-0.05Y after oxidation for 500 hours in air at 800°C

Table 1 The composition of the spinel phase located at 48 to 56 μm from the surface

Distance from the surface (μm)	O	Fe	Ni
	(at.%)		
48	56.0	32.6	11.4
50	55.1	33.2	11.7
52	55.6	32.8	11.6
54	55.4	32.7	11.9
56	55.4	32.7	11.9

A dense pellet with a composition of $Ni_{0.9}Fe_{2.1}O_4$ (similar to the spinel formed on Fe-Ni alloys as shown in Fig. 5(b) and Table 1) was prepared for electrical conductivity measurement. A linear relation between ln(σT) and 1/T was observed for $Ni_{0.9}Fe_{2.1}O_4$, as shown in Fig. 4. The electrical conductivity of $Ni_{0.9}Fe_{2.1}O_4$ was found to be higher than the stoichiometric $NiFe_2O_4$, most likely due to the creation of new charge carriers in the off-stoichiometric $Ni_{0.9}Fe_{2.1}O_4$. In addition, the electrical conductivity of $Ni_{0.9}Fe_{2.1}O_4$ was found to be orders of magnitude higher than that of the $Mn_{1.5}Cr_{1.5}O_4$ spinel (a composition similar to the spinel formed on Crofer after thermal oxidation) and single-crystal Cr_2O_3. These results indicated that the $(Fe,Ni)_3O_4$ spinel possessed excellent electrical conductivity; thus, the Fe-Ni alloys forming this spinel surface oxide are expected to have low scale electrical resistance, which was confirmed by ASR measurement of the oxidized coupons, as shown in this section later (e.g. see Fig. 11). We have also measured the electrical conductivities of $(Fe,Ni)_3O_4$ doped with different transition metals and reactive elements. It was found that Co, Mn, Y, or La addition further improved the electrical conductivity of the $(Fe,Ni)_3O_4$ spinel. As a result, alloying additions of these elements might reduce the scale ASR of the Fe-Ni alloys if they are incorporated into the spinel phase.

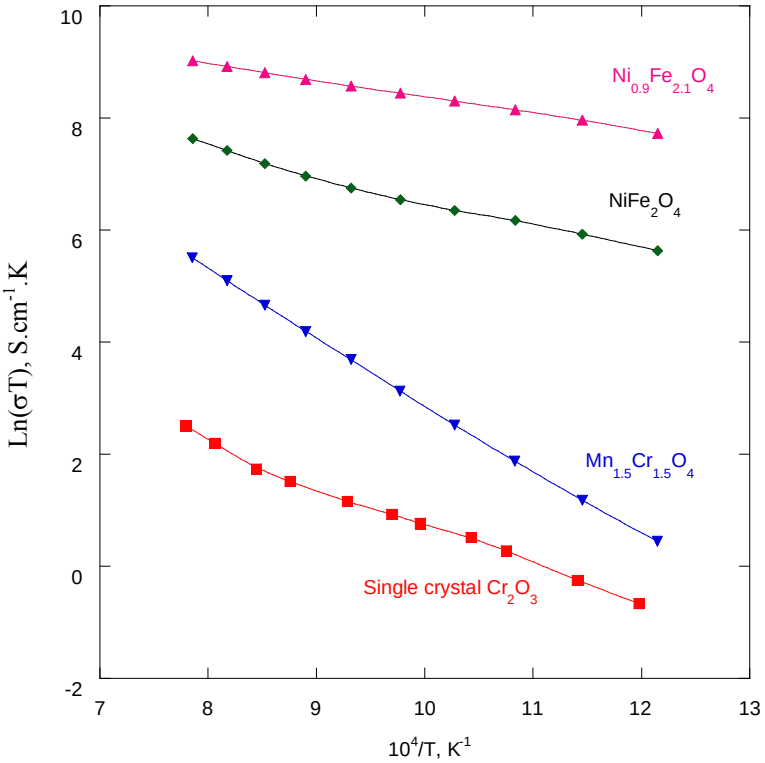

Fig. 6 Comparison of electrical conductivity of $(Fe,Ni)_3O_4$, $Mn_{1.5}Cr_{1.5}O_4$, and Cr_2O_3

The initial oxidation behavior of the Fe-50Ni-0.05Y alloy was studied using the thermobalance. The oxidation kinetics of Fe-50Ni-0.05Y in air at 700-900°C and in H_2+Ar+H_2O at 800°C was shown in Fig.7. It is clear that the mass gain in air (cathode environment) increased with the increase in oxidation temperature, while no weight change was observed in Ar+4%H_2 saturated with H_2O (simulated anode environment).

The surface morphologies of the samples after oxidation at different temperatures were presented in Fig. 8. The surface oxide nodules increased in size with the increase in oxidation temperature, while a relatively smooth surface with some thermal grooving was observed for the sample oxidized at 800°C in Ar+4%H_2 saturated with H_2O.

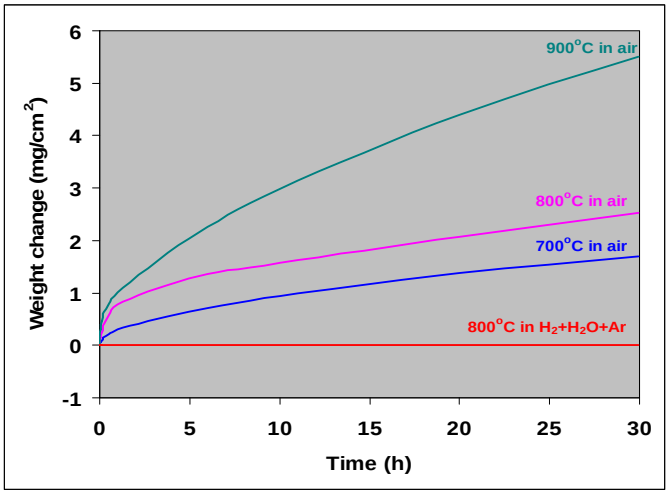

Fig.7 Oxidation kinetics of Fe-50Ni-0.05Y in both oxidizing and reducing atmospheres

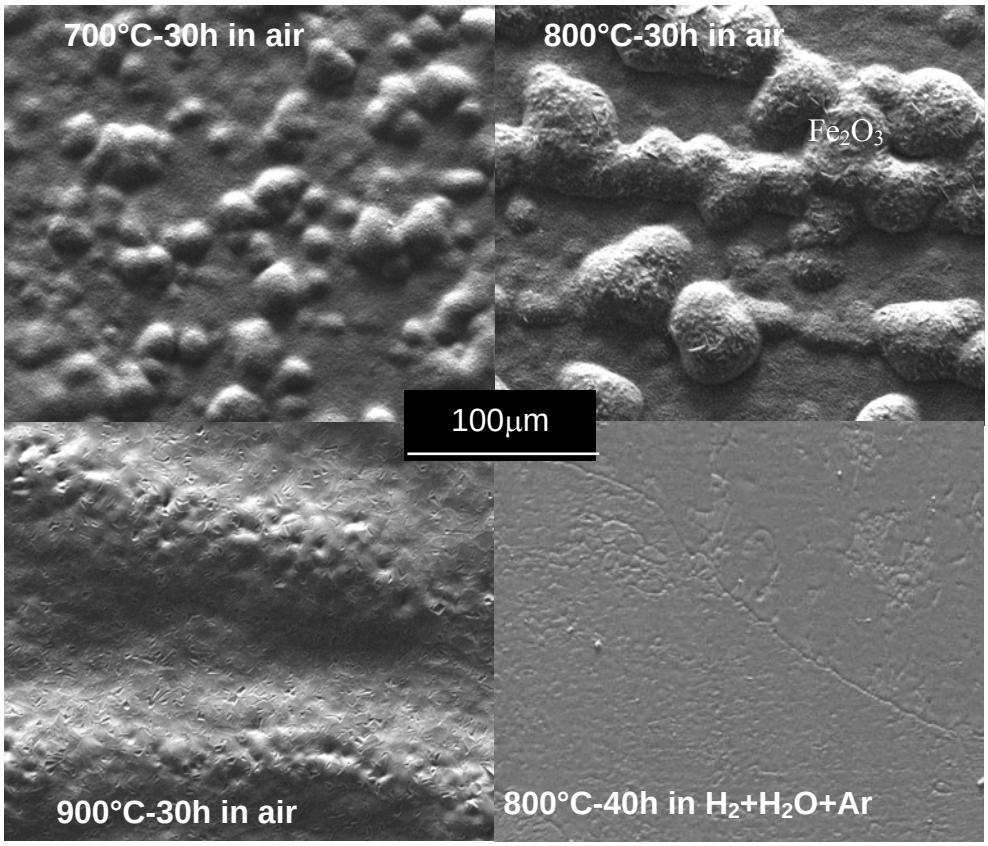

Fig.8 Surface morphologies of Fe-50Ni-0.05Y after short-term oxidation in air and in Ar+4%H_2 saturated with H_2O

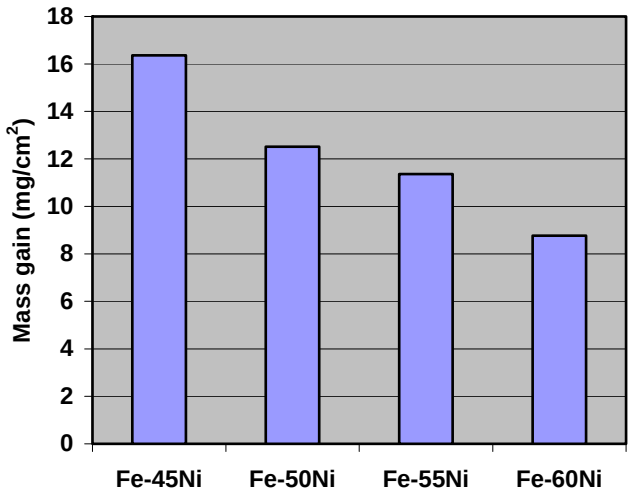

Fig.9 Mass gain of Fe-Ni alloys after oxidation for 500 hours in air at 800°C

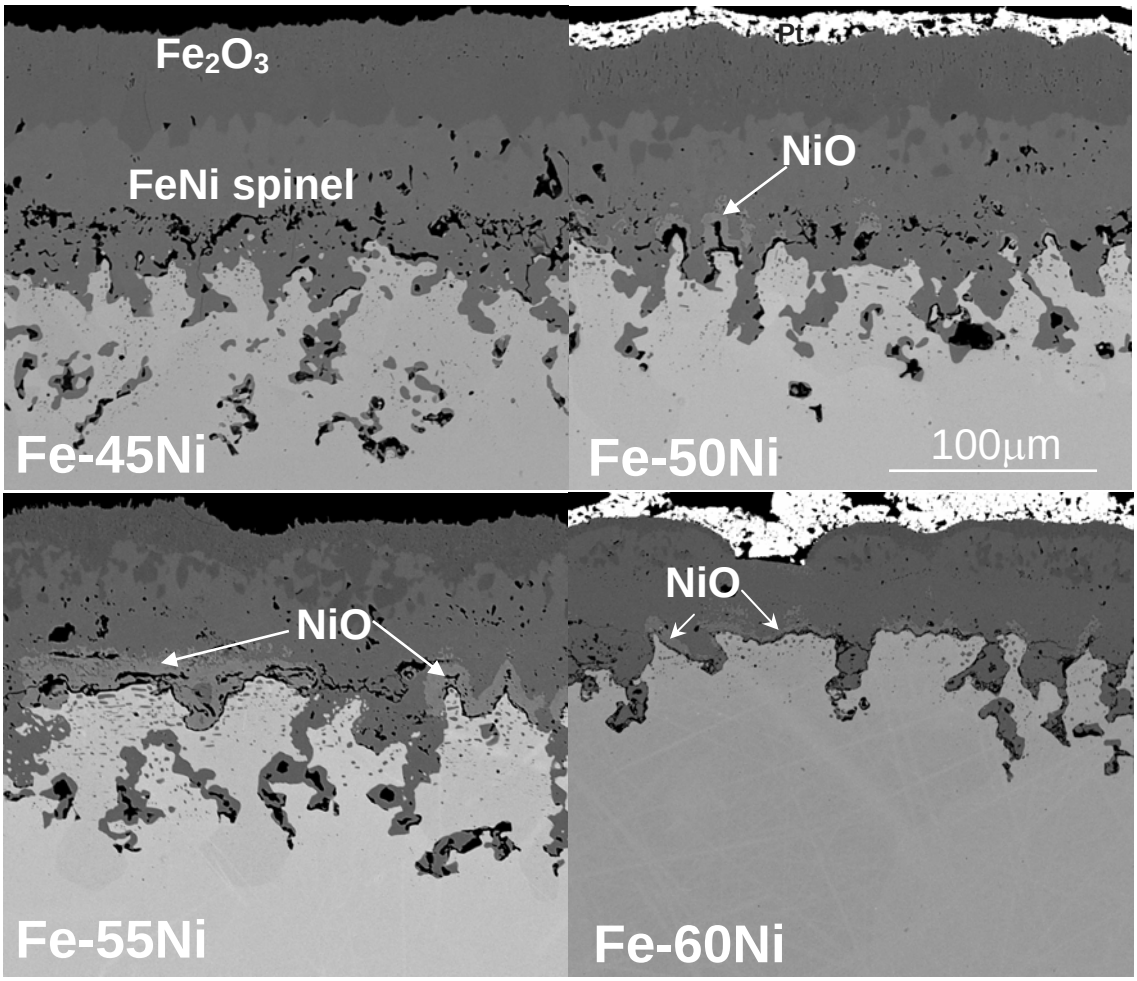

Fig.10 Cross-sections of the Fe-Ni alloys after oxidation for 500 hours in air at 800°C

Long-term oxidation behavior of the Fe-Ni binary alloys with different Ni contents was also studied in air at 800°C. Fig.9 presents the mass gain of Fe-Ni alloys with different Ni contents after isothermal oxidation for 500 hours in air at 800°C. The weight gain of alloys decreased with the increase in Ni content in alloys. This can be explained by the cross-sectional observation as shown in Fig.10. The oxide scale became thinner with the increase of Ni content in the alloys. The thickness of Fe_2O_3 layer also decreased with the increase of Ni content in the alloys. While no NiO sub-layer underneath the $(Fe,Ni)_3O_4$ spinel was formed on Fe-45Ni, NiO was observed between the spinel and substrate on Fe-50Ni, Fe-55Ni and Fe-60Ni. The continuity of the NiO layer improved with the increase in Ni content in alloys, as shown in Fig.10. Therefore, the enhancement of oxidation resistance of the higher Ni-content Fe-Ni binary alloys is most likely due to the formation of NiO layer between spinel and substrate.

As shown in Fig.11, the ASRs of the surface oxide scale grown on the binary Fe-Ni alloys after oxidation for 500 hours in air at 800°C decreased also with the increase in Ni content. Furthermore, the ASRs of the oxide scales on these alloys were comparable to those of current interconnect alloys such as Ebrite, Crofer and Haynes 230. The ASR of the oxide scales formed on Fe-45Ni was similar to that formed on Ebrite. The ASR of the oxide scale grown on Fe-50Ni was close to that of Crofer, while the ASR of the oxide scale formed on Fe-55Ni was lower than those of Ebrite and Crofer and slightly higher than that of Haynes 230. The ASR of the oxide scale formed on Fe-60Ni was lower than that of Fe-55Ni and similar to that of Haynes 230. Bearing in mind that the Fe-Ni alloys formed much thicker oxide scales than the current Cr-forming interconnect alloys, these results confirmed the superior electrical conductivity of the $(Fe,Ni)_3O_4$ spinel phase, as indicated in Fig. 6.

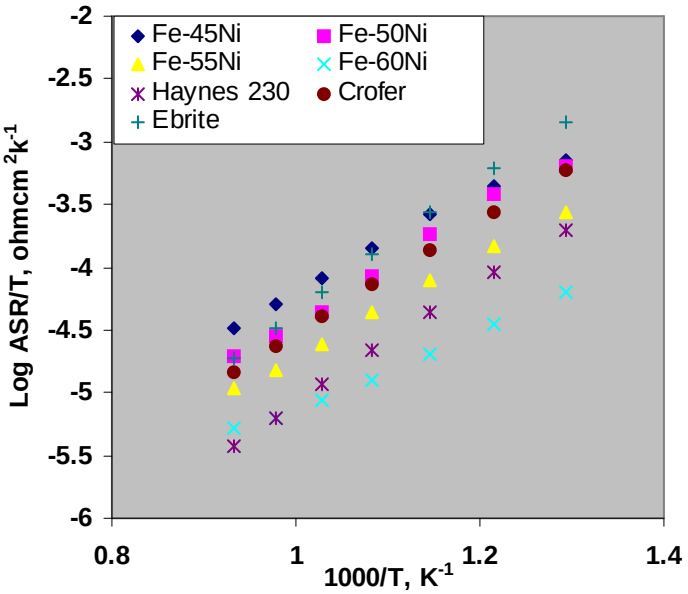

Fig.11 ASR of the oxide scale formed on the Fe-Ni alloys after oxidation for 500 hours in air at 800°C

From the above results, the CTEs of Fe-Ni binary alloys are close to those of major cell components and the electrical resistance of the oxide scale formed on them is quite low and comparable to those formed on current SOFC interconnects such as Ebrite, Crofer and Haynes 230. However, the oxidation resistance of these alloys is not adequate for SOFC interconnect application. Therefore, more emphasis has been placed on improving the oxidation resistance of these new Fe-Ni based alloys through alloy design. A promising low Cr Fe-Ni-Co based alloy has been identified as described in the next section.

4.2 Low Cr Fe-Ni-Co Based Alloy

Through a systematic alloy design effort, a low Cr Fe-Ni-Co based alloy with drastically improved oxidation resistance has been developed. While the exact composition of the alloy is not given here for intellectual property protection (a patent application has been initiated), this alloy is based on Fe-Ni-Co with 6%Cr, 3-6%X, 0.5-2.5%Y, and 0.05-0.2%Z (all in wt.%), where X denotes an element desirable for controlling the CTE and Y and Z are added mainly for improving the oxidation resistance of the alloy. An systematic evaluation of this alloy is summarized here. It should be noted that additional alloy composition modifications are expected to further optimize its overall performance.

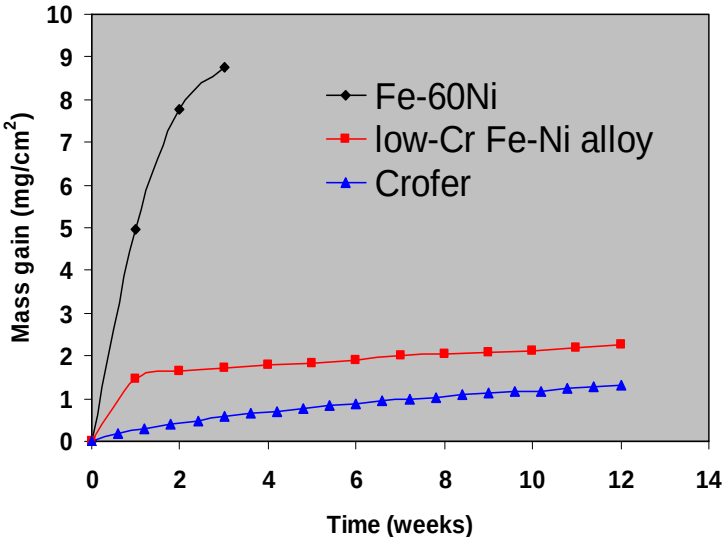

Fig.12 Oxidation kinetics of the alloys at 800°C in air

4.2.1 Oxidation Behavior and Oxide Scale ASR

Long-term isothermal oxidation test results indicated that the oxidation resistance of the new low Cr Fe-Ni-Co based alloy was much higher than that of Fe-60Ni, and comparable to that of Crofer. As shown in Fig. 12, after the 1st week, the weight gain of this low Cr alloy increased slightly with time and its oxidation rate was similar to that of Crofer. The initially larger weight gain during the 1st week exposure for this alloy over Crofer is exactly desirable, as it is due to the formation of a surface spinel outer layer. Compared to the binary Fe-60Ni alloy, an order of magnitude reduction in weight gain was achieved. The improved oxidation resistance of this new alloy resulted from the formation of a

continuous, dense Cr_2O_3 inner layer between the Cr-free spinel layer and substrate as shown in Figs. 13 and 14, which are the cross-sectional view and EPMA area mapping of Cr in this alloy after oxidation at 800°C in air, respectively.

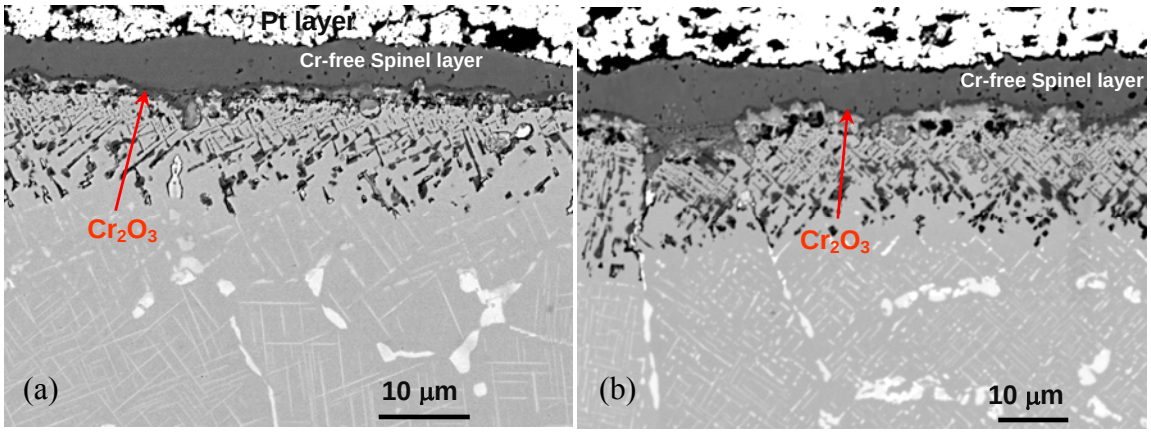

Fig.13 Cross-sections of the low Cr Fe-Ni-Co alloy after oxidation at 800C in air: (a) 3 weeks and (b) 12 weeks

The oxide scale thickness after oxidation for 3 weeks (Fig 13 (a)) was almost the same as that for 12 weeks (Fig.13 (b)), which was consistent with the oxidation kinetics as shown in Fig. 12. Fig.14 (a) is a backscattering image of the low Cr Fe-Ni-Co alloy after oxidation for 12 weeks at 800°C in air and Fig.14 (b) is the corresponding area mapping of Cr in the same area. Clearly, the spinel outer layer was completely free of Cr, which is therefore highly desirable to block the Cr evaporation from the Cr_2O_3 inner layer. Also from Fig. 14, the inner Cr_2O_3 scale was continuous and thus provided a barrier for oxygen penetration into the substrate. Between the Cr_2O_3 and substrate, some discrete oxide particles of mainly Cr_2O_3 were observed, due to the internal oxidation.

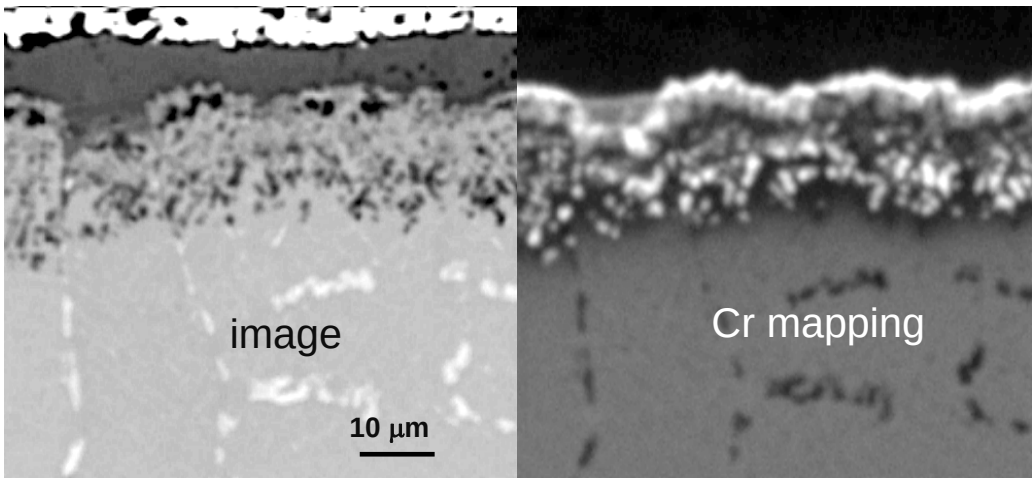

(a) (b)

Fig.14 Cross-section (a) and Cr mapping (b) of low Cr Fe-Ni-Co alloy after oxidation for 12 weeks at 800°C in air

XRD and EPMA line scan results in Figures 15 and 16 indicate that a $(Fe,Co,Ni)_3O_4$ spinel layer was developed on the low-Cr alloy during the early period of oxidation. Peaks of chromia were not observed from the XRD patterns of the thermally-grown oxide scale on the low-Cr alloy after oxidation for 3 weeks at 800ºC; both Cr_2O_3 and $CrNbO_4$ were detected upon lightly polishing off the outer surface oxide layer and repeating the XRD measurements. EPMA line analysis (Figure 16) again verified that the spinel top layer was essentially free of Cr, and a thin Cr-rich inner oxide layer was formed at the alloy/spinel interface after 3-week oxidation at 800ºC, consistent with the results shown in Fig. 14.

During the initial stage of oxidation, the scale consisted mainly of Fe, with some additional presence of Co and Ni, resulting in rapid weight gain and subsequent formation of the $(Fe,Co,Ni)_3O_4$ spinel layer as indicated in Figures 12 and 15. Following formation of the spinel layer, Cr was enriched near the substrate adjacent to the scale as a result of the depletion of Fe, Co and Ni at that location. The oxygen partial pressure at the spinel/alloy interface was decreased due to establishment of the surface spinel layer. As a result, selective oxidation of Cr was promoted, leading to the formation of a continuous chromia inner layer in contact with internal oxides of mainly Cr_2O_3 and $CrNbO_4$ (Figures 14-16). Furthermore, the Si and Nb significantly aided the formation of the chromium oxide via a secondary oxygen getter-type effect [20,21]. This inner layer served to effectively reduce the rate of oxidation, and slow down the continued growth of the outer spinel layer. Some Si enrichment in the internal oxidation zone was also evident in Figure 16 and might also have contributed to the reduced oxidation rate; however, continuous SiO_2 layer formation was not observed by SEM/EPMA analysis.

STEM observation of the oxide scale thermally grown on the low-Cr Fe-Ni-Co alloy after exposure to air at 800ºC for 3 weeks indicates the existence of a fine-grained Cr_2O_3 layer next to the spinel outer layer, as shown in Fig. 17(a), consistent with the EPMA results. There were, however, a number of oxides formed at the region between the internal oxidation zone and the alloy substrate, including Cr_2O_3, Nb-Ni-Co-Si-O, $CrNbO_4$, etc, as shown in Fig. 17(b). Furthermore, no continuous insulating layer of SiO_2 was detected across the oxide scale using STEM. This is in agreement with the low scale ASR for this alloy. It seems that Si was combined with some other metallic elements to form multi-component oxides. The electrical properties of the Si-containing oxides are currently not available.

As long as the Si-containing oxides are not interconnected to form a layer, the scale ASR will not be an issue. STEM study of an alloy sample thermally oxidized for 40 weeks at 800ºC in air also did not detect any SiO_2 layer formation. Also, based on STEM observation, the oxide scale features did not change significantly upon 40-week exposure, even though additional longer-term oxidation testing might be needed to further confirm this conclusion.

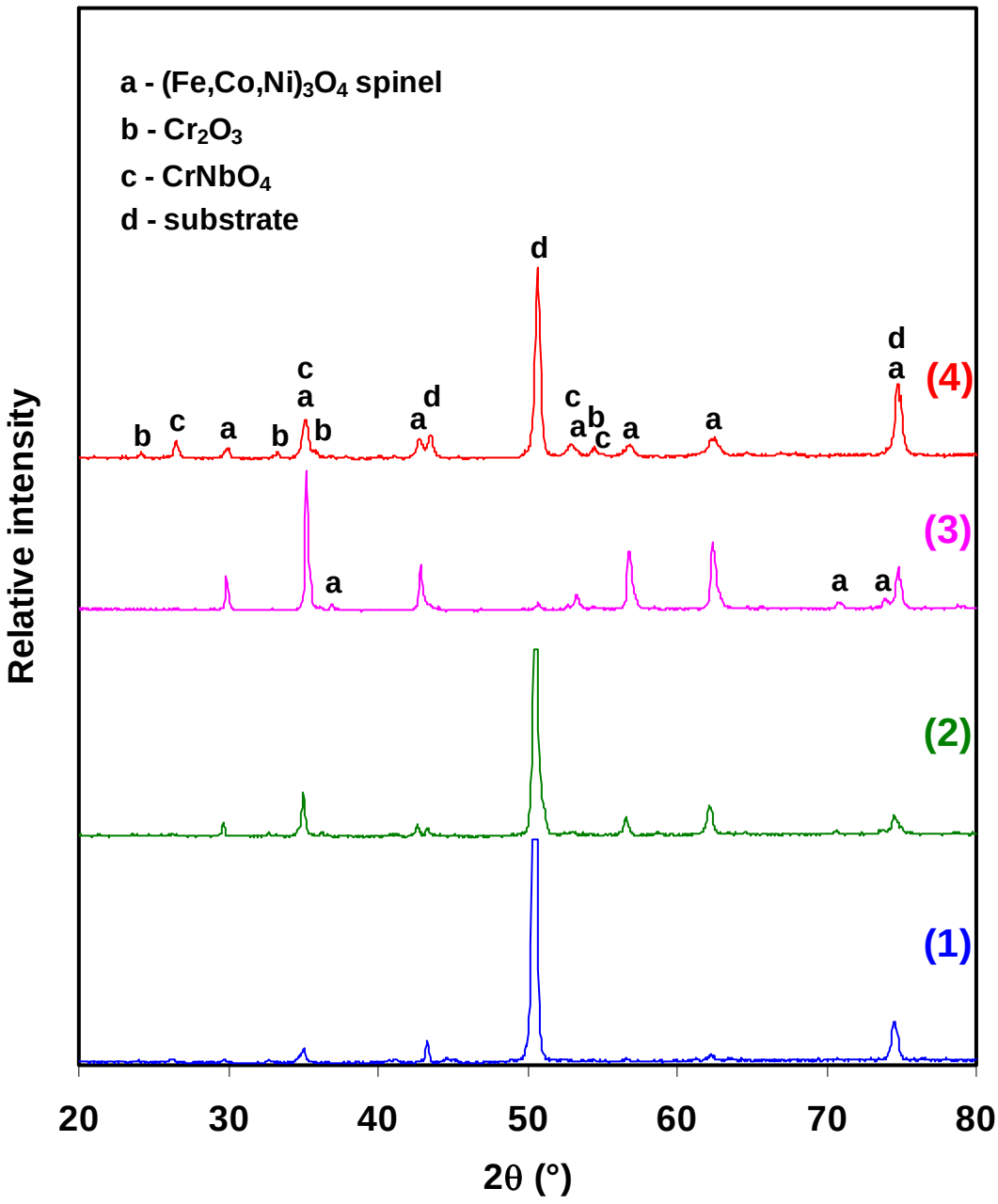

Fig. 15 XRD patterns of oxide scale formed on low-Cr Fe-Co-Ni alloy after oxidation in air at 800°C for (1): 5 hours; (2): 30 hours; and (3): 3 weeks (504 hours); respectively, (4): after the top oxide layer of (3) was partially polished off

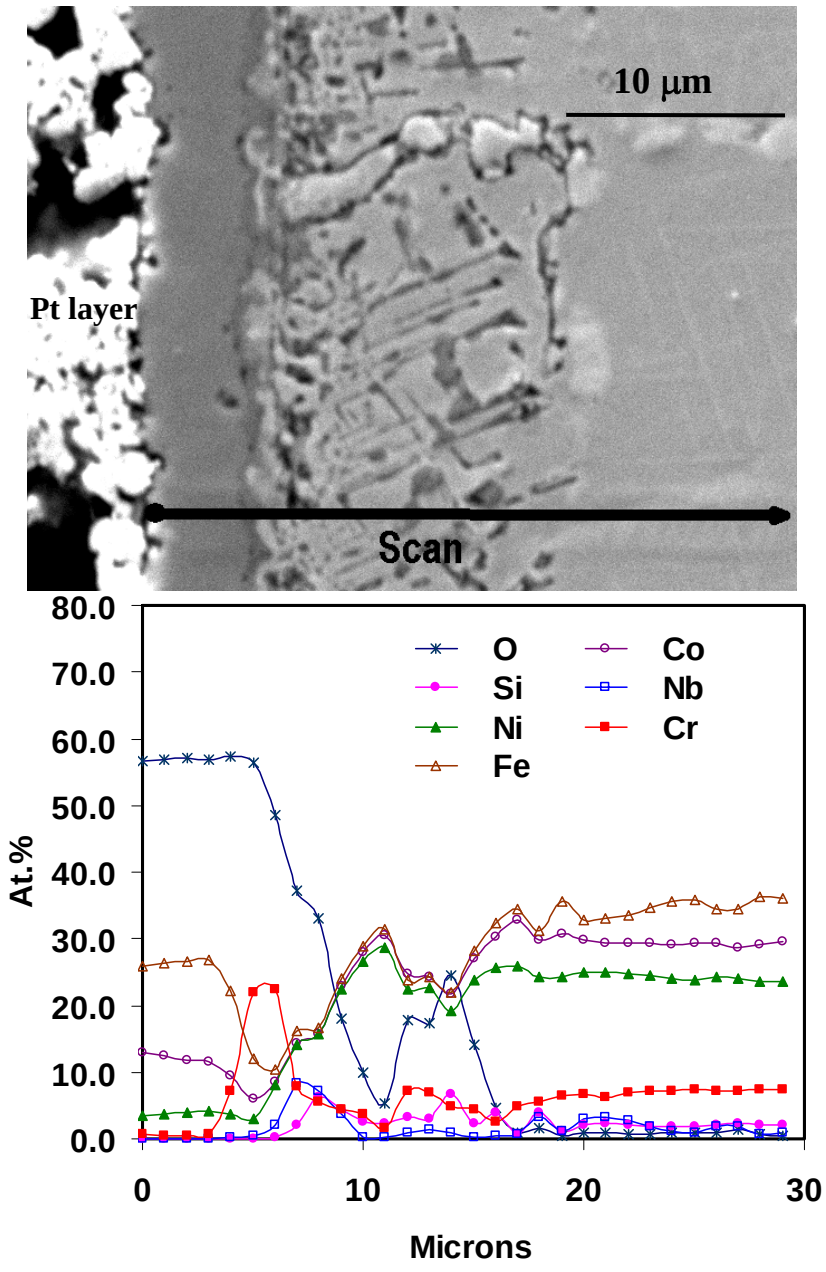

Fig. 16 EPMA results of the oxide scale formed on the low-Cr Fe-Co-Ni alloy after oxidation for 3 weeks in air at 800°C

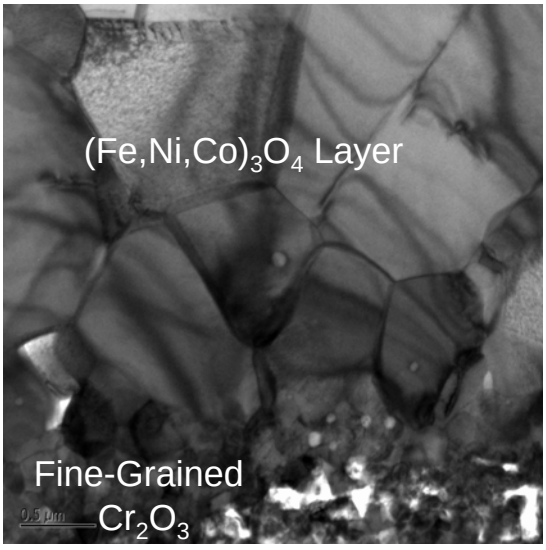

(a)

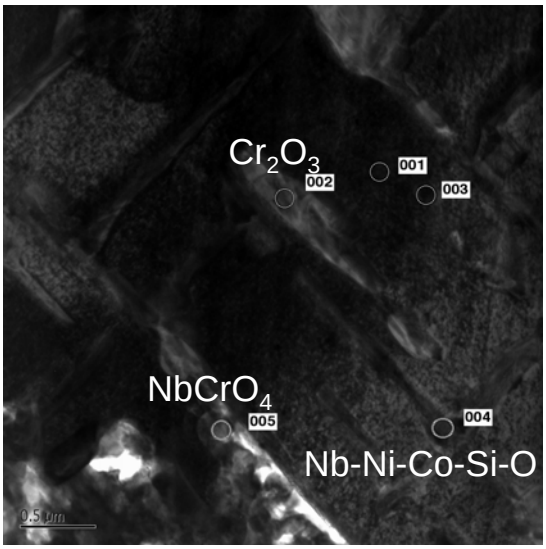

(b)

Fig. 17 STEM micrographs of the oxide scale formed on the new alloy after thermal oxidation for 3 weeks at 800ºC in air: (a) next to the spinel layer; (b) near the alloy surface.

One of the key requirements for SOFC interconnect materials is a relatively low and stable scale area specific resistance (ASR) for the interconnect alloys during cell operation. The scale ASR measurements were made on oxidized alloy coupons from 500 to 800ºC using the 4-point 2-probe method. The scale ASR for the new low-Cr Fe-Co-Ni alloy after oxidation for two different durations (3 and 12 weeks) in air at 800°C was compared with that for Crofer 22 APU under the same exposure conditions. As shown in Figures 12 and 18, even though the overall specific mass gain of the low-Cr alloy was

higher (thicker oxide scale) than that of Crofer 22 APU, its scale ASR was lower than that for Crofer 22 APU. Most noticeably, the scale ASR for the low-Cr alloy after oxidation for 12 weeks was almost the same as that for 3 weeks (Fig. 18), consistent with the oxidation kinetics shown in Figure 12 and clearly more stable than Crofer 22 APU.

This lower scale ASR for the low-Cr alloy over Crofer 22 APU is related to the different surface oxide structures formed on these two alloys. As shown in Fig. 13-17, the oxide scale developed on the new low-Cr alloy after oxidation at 800°C in air consisted of a $(Fe,Co,Ni)_3O_4$ spinel outer layer and a thin chromia inner layer; whereas, the oxide scale formed on Crofer 22 APU after oxidation in the same condition was comprised of a $(Mn,Cr)_3O_4$ outer layer and a relatively thick chromia-rich inner layer [15,21]. The lower scale ASR for the low-Cr alloy might be attributed to the higher electrical conductivity of $(Fe,Co,Ni)_3O_4$ compared to $(Mn,Cr)_3O_4$ and Cr_2O_3 [9,22] and/or the subsequently lower contact or interfacial resistance between $(Fe,Co,Ni)_3O_4$ and Pt (used for electrical contact in these experiments) compared to between $(Mn,Cr)_3O_4$ and Pt. Moreover, the chromia inner layer formed on the low-Cr alloy was thinner than that on Crofer 22 APU. It was also found that the scale ASR values were essentially the same prior to and after grinding/polishing of the four edges of the oxidized specimen, indicating that the electrical conduction was through the specimen thickness and not around the edges.

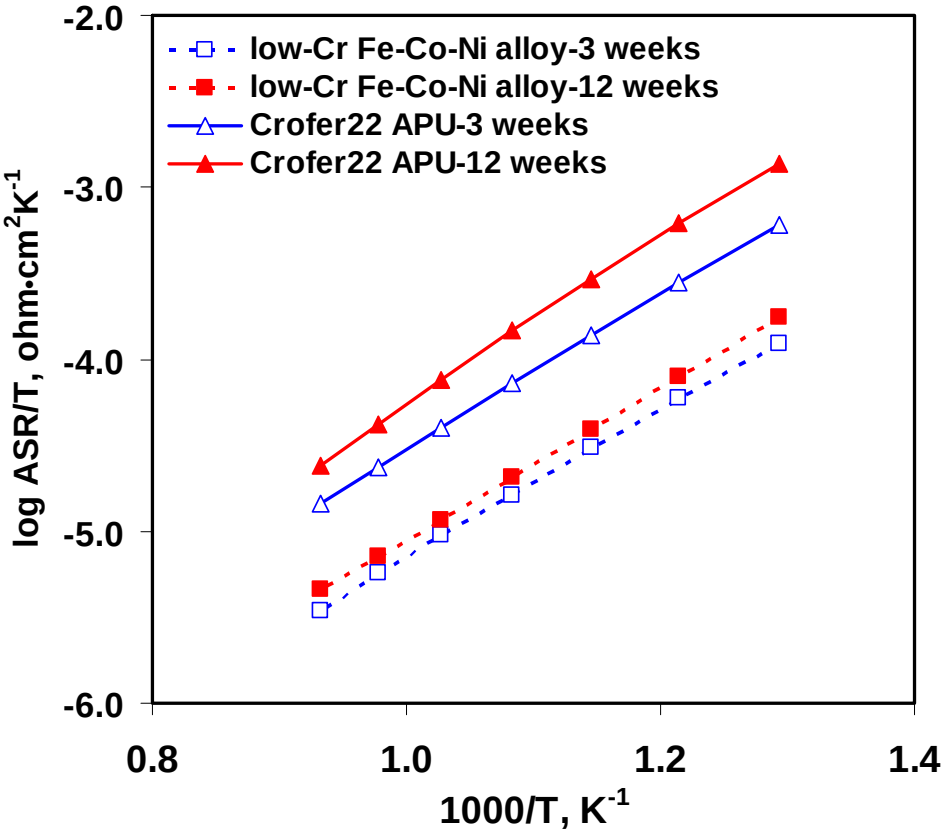

Fig. 18 Scale ASR for the low-Cr Fe-Co-Ni alloy after oxidation for 3 and 12 weeks in air at 800°C, as compared to that for Crofer 22 APU

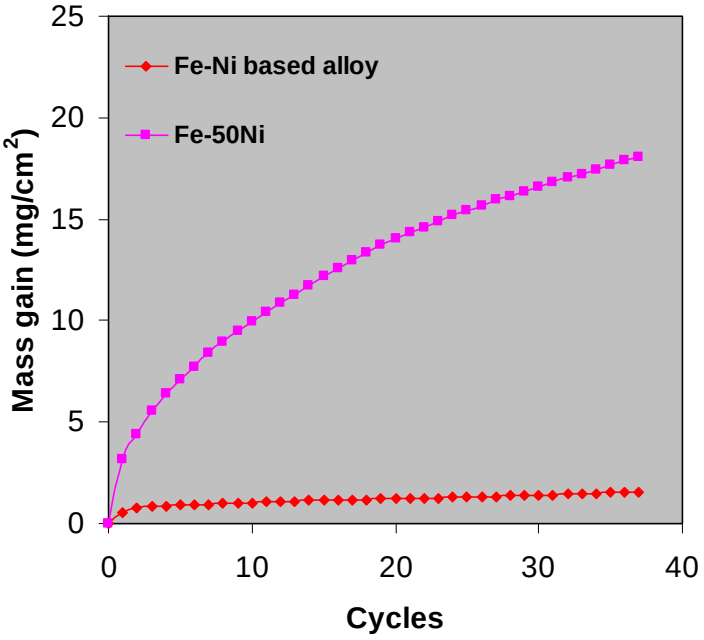

Fig.19 Cyclic oxidation kinetics of low-Cr Fe-Ni-Co alloy and Fe-50Ni at 800°C in air

Cyclic oxidation testing was also conducted to evaluate the oxide scale spallation resistance of the new low-Cr alloy. Each cycle consisted of holding at 800°C for 25 hours, followed by air cooling to room temperature. As shown in Figure 8, continual specific mass gains were observed for both the new alloy and the Fe-50Ni control alloy; furthermore, the oxidation resistance of the low-Cr alloy was drastically improved over the Fe-50Ni alloy, consistent with the isothermal oxidation results shown in Figure 12. After 80 cycles, no scale spallation was detected for either alloy. The excellent scale spallation resistance for these alloys is a result of the close match in CTE between the substrate and the surface spinel phase, which is expected to lead to low thermal stresses during thermal cycling for these alloys [23].

4.2.2 Thermal Expansion Behavior and Compatibility with Cathode Materials

Thermal expansion behavior of the new low Cr Fe-Ni-Co based alloy is shown in Fig. 20. Although the slope of the CTE curve of the new alloy increased with temperature above 400°C, it still exhibited an overall good match in thermal expansion behavior with other major cell components such as the electrolyte, cathode and anode over the temperature range of 100-800°C.

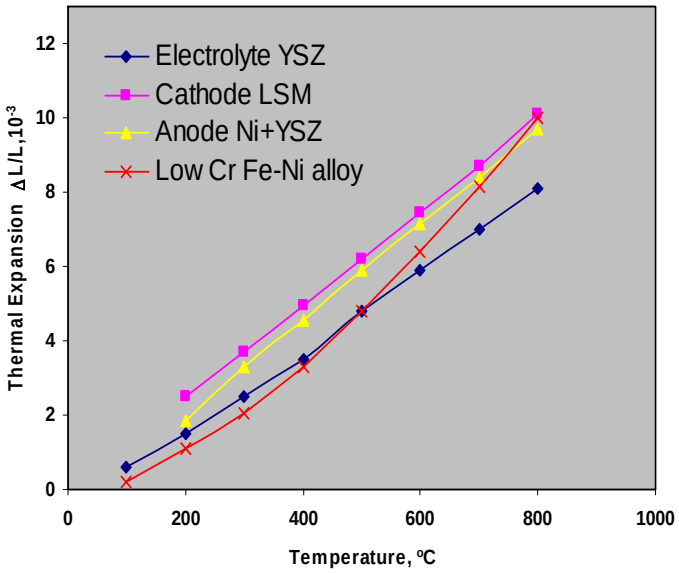

Fig.20 Thermal expansion vs. temperature for the low Cr Fe-Ni-Co alloy, as compared to other cell components

The thermal expansion behaviors of two spinel phases $Fe_{0.9}Ni_{2.1}O_4$ and $Cr_{1.5}Mn_{1.5}O_4$ were also determined, as shown in Fig.21. These two compositions were selected to represent the spinel outer layers formed on the Fe-Ni-Co alloys and the ferritic alloy Crofer 22 APU. Clearly, $Ni_{0.9}Fe_{2.1}O_4$ exhibited an excellent match in CTE with the Fe-Ni-Co alloy substrates as well as the other cell components, while $Cr_{1.5}Mn_{1.5}O_4$ had a much lower CTE compared to the Fe-Ni alloys (and also Crofer). The close match in CTE between the substrate and the $Ni_{0.9}Fe_{2.1}O_4$ spinel is expected to result in low residual thermal stresses during thermal cycling for the Fe-Ni-Co alloys; this is consistent with the cyclic oxidation results showing excellent scale spallation resistance for the Fe-Ni base alloys.

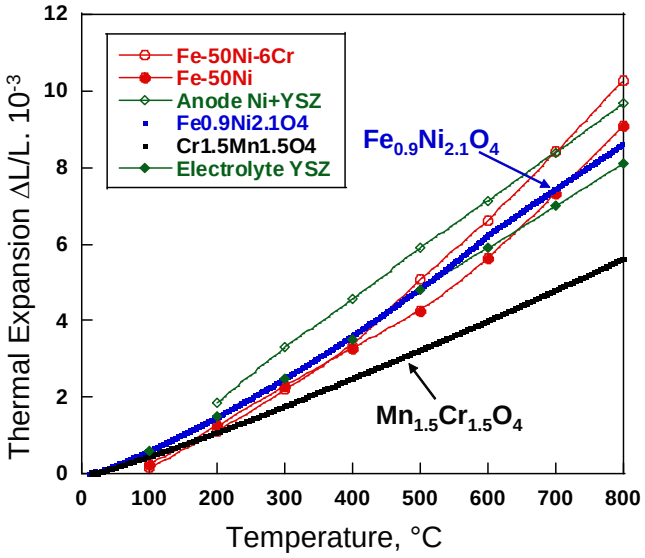

Fig.21 Thermal expansion vs. temperature for two spinel phases

Initial testing of the compatibility between the new Fe-Ni-Co based alloys and the cathode material LSM was carried out on the alloy/cathode couples fabricated by screen printing. After thermal exposure in air at 900°C for 300 hours, no obvious interaction or interdiffusion was observed between oxide scale and LSM layer, as shown in Fig.22. From Fig. 22(a)-(c), it is clear that the desired double-layer oxide scale was formed between the alloy substrate and the cathode paste. The outer layer was a Cr-free spinel rich in Fe and Ni, while the inner layer was Cr_2O_3. Also, no Cr migration into the cathode layer was detected, Fig.22 (c).

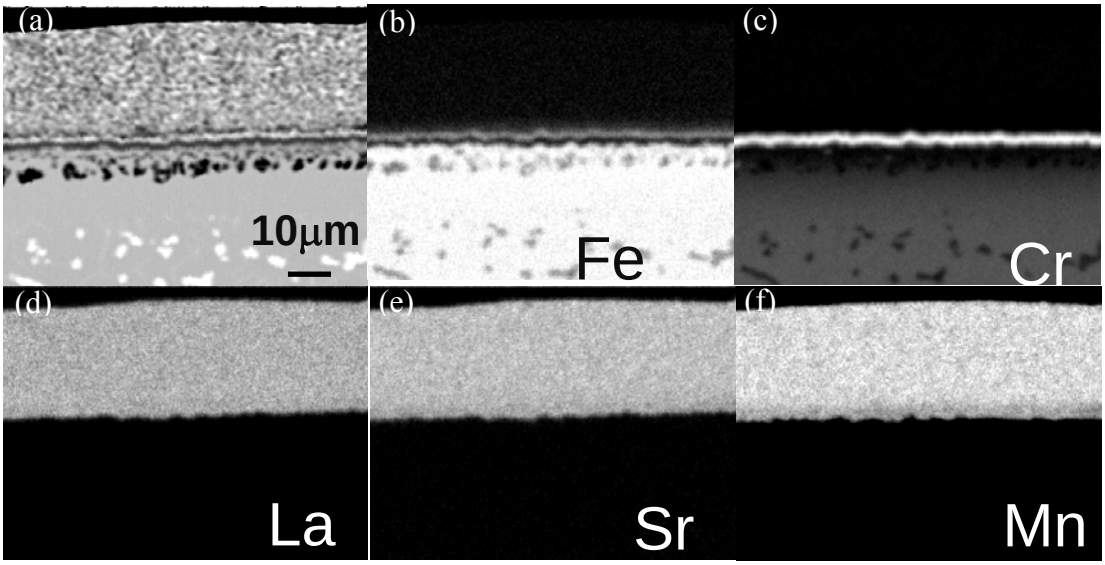

Fig. 22 Cross-section of the low-Cr Fe-Ni alloy/cathode couple after oxidation for 300 hours at 900°C in air: (a) backscattering image; (b) Fe mapping; (c) Cr mapping; (d) La mapping; (e) Sr mapping; and (f) Mn mapping

After thermal exposure, the ASR of the alloy/cathode coupons was also measured using the 2-probe, 4-wire technique. As shown in Fig. 23, the ASR of the low Cr Fe-Ni-Co alloy/LSM couple was lower than that of Fe-50Ni/LSM or Crofer/LSM couple after similar exposure. This result implies that no new insulating phase was formed between the cathode and the new Fe-Ni alloy. The lower ASR for the new Fe-Ni alloy might again be attributed to the formation of a higher electrically-conductive spinel layer between the cathode and the alloy substrate. The higher ASR for the Fe-50Ni/LSM couple was due to the extensive oxidation of the substrate alloy at such a higher exposure temperature. Longer-term thermal exposure is needed to confirm these initial results.

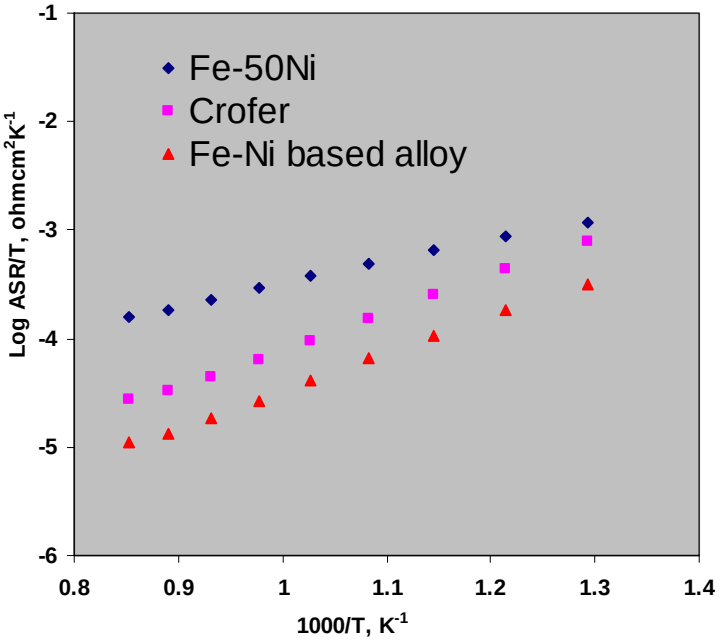

Fig.23 ASR of the new Fe-Ni-Co alloy/LSM couple after oxidation for 300 hours at 900°C in air, as compared to that of the Fe-50Ni/LSM and Crofer/LSM couples

4.2.3 Cr Transport Measurement and In-Cell Test Results

The rapid formation of the Cr-free spinel outer layer prior to the establishment of the chromia inner layer is expected to effectively reduce the Cr volatile species such as CrO_3 and $CrO_2(OH)_2$ originating from the chromia inner layer. This was confirmed by quantitative Cr volatility measurements in moist air at 800°C for 500 hours and an air velocity of 1.1 $cm \cdot s^{-1}$. The Cr transport rate was calculated to be 5.7×10^{-12} $kg \cdot m^{-2} \cdot s^{-1}$ for the low-Cr alloy. For comparison, under identical conditions a value of $3.3\times10^{-11} kg \cdot m^{2} \cdot s^{-1}$ was obtained for Crofer 22 APU. Thus, the Cr volatility for the low-Cr alloy was about a factor of 6 lower than that for Crofer 22 APU, the state-of-the-art ferritic alloy which forms $(Mn,Cr)_3O_4$ spinel overlying Cr_2O_3. The effective reduction in Cr transport rate for the low-Cr alloy as compared to Crofer 22 APU results from the differences in the surface oxide formation sequence as well as the Cr content/activity in the surface spinel for these two alloys.

For Crofer 22 APU, significant quantities of Cr are involved in the early stage of oxidation [24,25]. A Cr-containing spinel outer layer was formed and chromium vaporization from the $(Mn,Cr)_3O_4$ spinel layer was detected in spite of the relatively low thermodynamic activity of Cr in $(Mn,Cr)_3O_4$ [16], which could potentially lead to Cr migration to, and accumulation at, the cathode over long-term stack operation. This alloy was designed to balance a number of properties, including oxidation resistance, scale ASR, formability, cost, and Cr volatility. Even though a reduced Cr volatility was obtained compared to other chromia-forming alloys, this alloy was intended to be used with a Cr-blocking surface coating. For example, a Cr-free protection layer of

$Mn_{1.5}Co_{1.5}O_4$ spinel was synthesized on Crofer 22 APU via slurry coating technology, which acted effectively as a barrier to outward migration of Cr and therefore resulted in a stable electrochemical performance of SOFCs [25]. However, a coating process would increase the overall cost of the interconnect material, and its long-term stability is yet to be demonstrated. In the present work, a Cr-free surface spinel layer is formed *in situ* during the initial stages of oxidation, such that a coating is not necessary.

Cell performance stability with the Crofer and the new alloy (both in the bare and preoxidized conditions) is shown in Fig. 24. For the two bare alloys, an initial severe reduction in power density was observed, which is comparable for the two alloys. The power density continued to decrease with time, even though the degradation rate slowed down with time. The power density decrease can be attributed to the "so-called" Cr poisoning effect, i.e. Cr migration from the Cr-containing interconnect alloy to the LSM cathode, leading to a decrease in cathode electrochemical activity and thus cell performance reduction. While both the alloys exhibited a similar trend, it is noticed that the cell performance with the new alloy started to stabilize after about 120-hour operation, which is believed to be due to the *in-situ* formation of the Cr-free $(Fe,Ni,Co)_3O_4$ spinel layer on the alloy surface. The formation of this outer layer blocked the Cr evaporation from the alloy, resulting in a more stable cell performance. For one specific cell, preoxidation of the new alloy at 800ºC in air for 120 hours was conducted to form the spinel layer on the alloy interconnect prior to cell testing. The results, also shown in Fig. 24, implies that with the preoxidation treatment, the initial cell performance degradation was avoided; furthermore, the power density of the cell after 150-h testing remained as a high as 0.2 w/cm^2 at a fixed cell voltage of 0.7 V, which is much higher than that of the bare alloy (i.e. 0.05 w/cm^2). The scatter in the data for the preoxidized Fe-Ni-Co alloy is presumably due to some fuel leakage/cell sealing problems apparently associated with this cell.

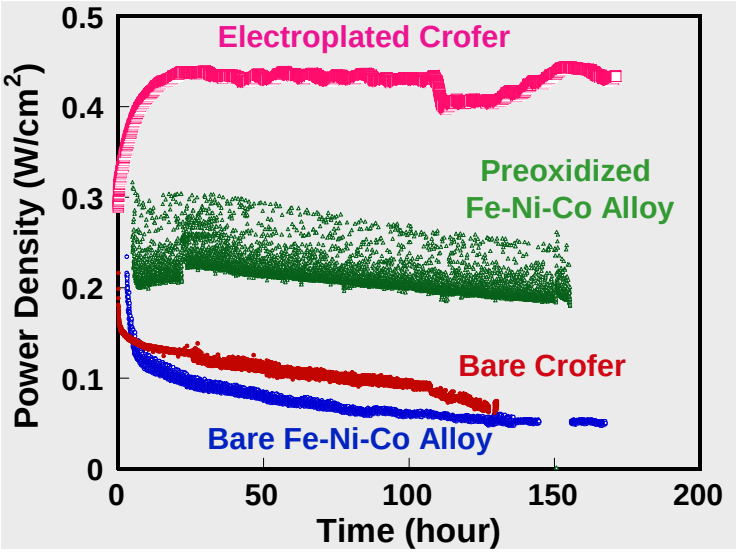

Fig. 24 The cell power density vs. cell operation time for several cells with different interconnects, including bare Crofer-22 APU and Co-Fe electroplated Crofer-22 APU, bare and preoxidized Fe-Ni-Co alloy.

The best cell performance stability, however, was observed when the electroplated Crofer-22 APU as interconnect. The electroplated Co-Fe layer on Crofer-22 APU significantly improved the cell performance stability as compared to the bare Crofer-22 APU as well as the newly-developed low-Cr Fe-Ni-Co alloy, as also shown in Fig. 24. This clearly demonstrated the effectiveness of the electroplated layer in blocking the Cr migration and poisoning. The surface $CoFe_2O_4$ layer could be observed on the interconnect surface after cell testing and no Cr could be detected in the surface oxide layer formed on interconnect as well as in the LSM cathode. More specifically, the oxide scale on Crofer-22 APU interconnect deposited with the Co-Fe film consisted of a 50-μm Cr-free $CoFe_2O_4$ spinel outer layer and a 10-μm Cr_2O_3 inner layer in contact with the Crofer-22 APU substrate. The Co-Fe layer was converted into a $CoFe_2O_4$ spinel layer during the cell testing. The formation of the Cr-free spinel blocked Cr transport from the substrate alloy, thus drastically improved the cell performance stability.

4.2.4 Tensile Properties

Tensile properties of the new alloy were plotted in Fig. 25 as a function of test temperature. The data for Crofer was included for comparison [26]. As shown in Fig. 25(a), the new alloy exhibited a ductility similar to Crofer from room temperature to 600ºC; however, Crofer possessed a slightly higher ductility as the temperature increased to over 600ºC. The overall good ductility of this new alloy is in agreement with the relative ease in fabricating this alloy into sheet via hot-rolling and cold-rolling, which might also lead to the possibility of additional forming operations such as stamping to process corrugated interconnect components.

The yield strength and tensile strength of the new alloy, however, were significantly higher than those of Crofer over the entire temperature range, as shown in Fig. 25(b). The higher strength of this new alloy might lead to better creep resistance; as a result, thinner interconnect plates might be used in SOFC stacks, thus reducing the raw material usage and the overall cost of the interconnect material.

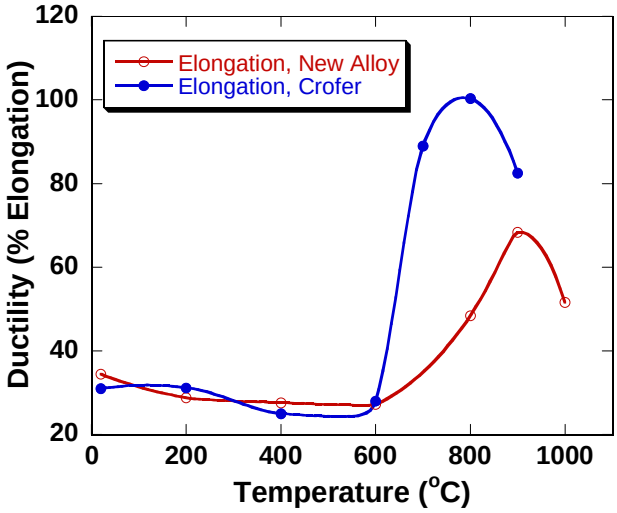

(a)

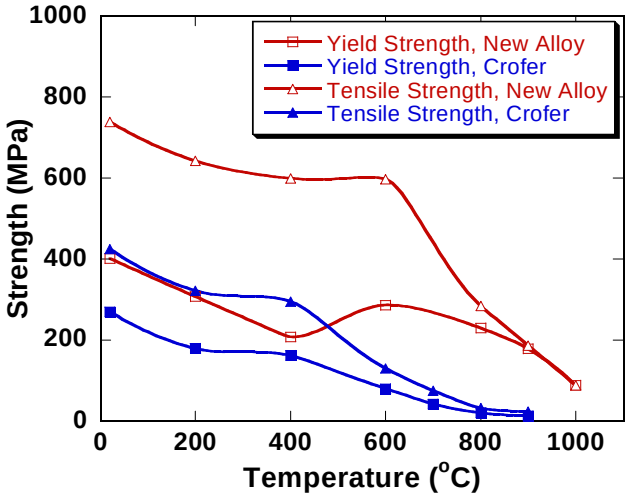

(b)

Fig. 25 Tensile properties of the new alloy and Crofer as a function of temperature: (a) ductility; and (b) yield strength and tensile strength.

5. Concluding Remarks and Suggested Future Works

The formation of an electrically conductive, Cr-free spinel outer layer atop a protective, electrically conductive oxide inner layer on the metallic alloys is highly desirable to mitigate the Cr poisoning problem in the SOFC stack. Our results indicate that although the CTEs and oxide scale ASRs of Fe-Ni binary alloys are suitable for the SOFC interconnect application, their oxidation resistance is not adequate and needs further improvement. A double-layer oxide structure with an electrically conductive, Cr-free spinel outer layer and a protective Cr_2O_3 inner layer was thermally grown on a new low Cr Fe-Ni-Co based alloy with drastically improved oxidation resistance, low Cr volatility and scale ASR, good CTE match with other cell components, adequate mechanical property as well as good compatibility with the cathode materials. The new low-Cr alloy is a promising alternative to replace high-Cr ferritic alloys as interconnect for IT-SOFCs.

While additional alloy design and production scale-up are clearly needed, this study has demonstrated that it is feasible to develop a low-Cr Fe-Ni-Co alloy with balanced properties for SOFC interconnect application. Since this alloy system contains significant amounts of Ni and Co than ferritic steels, it is suggested that this Fe-Ni-Co alloy system be combined with the ferritic steel to form a unique coating/alloy system as SOFC interconnect material. Furthermore, it is suggested that low-cost coating processes such as electroplating should be developed for achieving such a coating/alloy system. A new interconnect material with an electroplated surface layer of the Fe-Ni-Co alloy over the ferritic steel will combine the attributes of both the new Fe-Ni-Co alloy and the low-cost ferritic steels. The surface Fe-Ni-Co layer will be converted into a Cr-free, electrically-conductive $(Fe,Ni,Co)_3O_4$ spinel layer during thermal oxidation or SOFC

operation. The formation of this spinel layer is expected to reduce the oxygen penetration into the ferritic steel substrate (thus improving its oxidation resistance) and act as a surface seal to block the Cr evaporation and migration (thus mitigating the Cr evaporation problem of the ferrittic substrate). Initial cell testing results are very encouraging and significantly improved cell performance stability has been demonstrated for such a coating/alloy system.

It is further suggested that the future focus of our SECA interconnect project be redirected from alloy design to coating development. The new interconnect material system (FeNiCo-coated ferritic steels) is expected to reduce the overall material cost and improve the durability of SOFC stacks, thus contributing to early commercialization of the SOFC technology.

6. List of Publications Based on This Work

1. J.H. Zhu, S.J. Geng, Z.G. Lu, and W.D. Porter, "Evaluation of Binary Fe-Ni Alloys as Intermediate-Temperature SOFC Interconnect", *Journal of the Electrochemical Society*, 154(12), B1288, 2007.
2. S.J. Geng, J.H. Zhu, M.P. Brady, H.U. Anderson, X.D. Zhou, and Z.G. Yang, "A low-Cr metallic interconnect for intermediate-temperature solid oxide fuel cells", *Journal of Power Sources*, 172, p.775, 2007.
3. J.H. Zhu, S.J. Geng, and D.A. Ballard, "Evaluation of Several Low Thermal Expansion Fe-Co-Ni Alloys as Interconnect for Reduced-Temperature Solid Oxide Fuel Cell", *International Journal of Hydrogen Energy*, 32, p.3682, 2007.
4. Z.G. Lu, J.H. Zhu, Y. Pan, N. Wu, and A. Ignatiev, "Improved oxidation resistance of a nanocrystalline chromite-coated ferritic stainless steel", *Journal of Power Sources*, in press, 2008.

7. Acknowledgements

This research was sponsored by the DOE SECA Core Technology Program (DOE Award #DE-FC26-04NT42223). Additional support was provided by the Center for Manufacturing Research, Tennessee Technological University.

8. References

1. S. Linderoth, P.V. Hendriksen, M. Mogensen, and N. Langvad, J. Mat. Sci., 31, p.5077 (1996).
2. P.Y. Hou, K. Huang, and W.T. Bakker, in Solid Oxide Fuel Cells VI, p.737, S.C. Singhal and M. Dokiya, eds., ECS, Pennington, NJ, USA, 1999.
3. S. Linderoth and P.H. Larsen, in New Materials for Batteries and Fuel Cells, p.325, MRS Symp. Proc. Vol. 575, MRS, Warrendale, PA, USA, 2000.
4. K. Huang, P.Y.Hou, and J.B. Goodenough, Solid State Ionics, 129, p.137 (2000).
5. T. Harita, Y. Xiong, K. Yamaji, N. Sakai, and H. Yokokawa, J. Electrochem. Soc., 150, p.A243 (2003).

6. Z. Yang, K.S. Weil, D.M. Paxton, and J.W. Stevenson, J. Electrochem. Soc., 150, p.A1188 (2003).
7. T. Kadowaki, T. Shiomitsu, E. Matsuda, H. Nakagawa, and H. Tsuneizumi, Solid State Ionics, 67, p.65 (1993).
8. W.J. Quadakkers, T. Malkow, J. Pirón-Abellán, U. Flesch, V. Shemet, and L. Singheiser, in Proceedings of the Fourth European Solid Oxide Fuel Cell Forum, p.827, A.J. McEvoy, Lucerne, Switzerland, 2000.
9. W.Z. Zhu and S.C. Deevi, Mat. Res. Bulletin, 38, p.957 (2003).
10. W.Z. Zhu and S.C. Deevi, Mat. Sci. Eng., A348, p.227 (2003).
11. K. Hilpert, D. Das, M. Miller, D.H. Peck, and R. Weiβ, J. Electrochem. Soc., 143, p.3642 (1996).
12. Y. Matsuzaki and I. Yasuda, Solid State Ionics, 132, p.271 (2000).
13. W.J. Quadakkers, J. Piron-Abellan, V. Shemet, and L. Singheiser, Mater. High Temp., 20(2), p.115 (2003).
14. F. Tietz, Mat. Sci. Forum, 426-432, p.4465 (2003).
15. Z. Yang, J.S. Hardy, M.S. Walker, G. Xia, S.P. Simner, and J.W. Stevenson, J. Electrochem. Soc., 151, p.A1825 (2004).
16. C. Gindorf, L. Singheiser and K. Hilpert, Steel Res., 72(11/12), p.528 (2001).
17. J. H. Zhu, unpublished results, Tennessee Technological University, 2008.
18. L. A. Chick, L. R. Pederson, G. D. Maupin, J. L. Bates, L. E. Thomas and G. Exarhos, Materials Letters, 10, p.6 (1990).
19. J.H. Zhu, Y. Zhang, A. Basu, Z.G. Lu, M. Paranthaman, D.F. Lee, and E.A. Payzant, Surface & Coatings Tech., 177/178, p.65 (2004).
20. J.M. Oh, J. Electrochem. Soc., 135(3) p. 749 (1988).
21. S.J. Geng, J.H. Zhu, and Z.G Lu, Solid State Ionics, 177 (5-6), p. 559 (2006).
22. H. Ling and A. Petric, Electrochemical society proceedings 2005-07, p. 1866 (2005).
23. J.H. Zhu, S.J. Geng, Z.G. Lu, and W.D. Porter, J. Electrochem. Soc., 154, p.B1288 (2007).
24. Z. Yang, G.G., Xia, S.P. Simner, and J.W. Stevenson, J. Electrochem. Soc., 152(9), p.A1896 (2005).
25. S.P. Simner, M.D. Anderson, G.G. Xia, Z. Yang, L.R. Pederson, and J.W. Stevenson, J. Electrochem. Soc., 152(4), A740-A745 (2005).
26. R. Hojda and L. Paul, NACE Paper No. 6479, in Corrosion 2006 (2006).